Article

Influence of Al and N Content and Cooling Rate on the Characteristics of Complex MnS Inclusions in AHSS

Muhammad Nabeel *, Michelia Alba and Neslihan Dogan

Department of Material Science and Engineering, Faculty of Engineering, McMaster University, 1280 Main Street West, Hamilton, ON L8S 4L7, Canada; albam@mcmaster.ca (M.A.); dogann@mcmaster.ca (N.D.)

* Correspondence: nabeelm@mcmaster.ca

Abstract: This study focused on the characteristics of complex MnS inclusions in advanced high strength steels. The effect of metal chemistry (Al and N) and the cooling rate of steel were evaluated by analyzing the inclusions present in five laboratory produced steels. The observed complex MnS inclusions contained Al_2O_3-MnS, AlN-MnS, and AlON-MnS. An increase in Al content from 0.5% to 6% increased the number of complex MnS inclusions by ~4 times. In comparison, a decrease of ~80% was observed due to the increased N content of steel from <10 ppm to ~50 ppm. MnS precipitation ratio was used to determine the potency of different inclusions forming complex MnS inclusions due to heterogeneous nucleation. It was found that the MnS precipitation ratio of the observed inclusions was related to their misfit with MnS, and it decreased in the order of AlN > AlON > Al_2O_3. Moreover, it was determined that AlN particles could be easily engulfed at the solidification front relative to Al_2O_3, which resulted in a higher MnS precipitation ratio for Al_2O_3 under slow cooling conditions.

Keywords: complex MnS; heterogeneous nucleation; precipitation ratio; engulfment and pushing; misfit; AlN inclusions

---

1. Introduction

An excellent combination of high strength, high toughness, and lightweight of advanced high strength steels (AHSS) makes them suitable for various applications. AHSS contain high concentrations of alloying elements such as Mn, Al, and Si. Therefore, these steels are likely to have a large number of inclusions having a range of compositions. There has been thorough research on the microstructure and mechanical properties of AHSS [1–8], while knowledge related to non-metallic inclusions in AHSS is still limited. Previous studies [9–15] on non-metallic inclusions have identified the primary type of inclusions as MnS, Al_2O_3, and AlN. The presence of Al_2O_3-MnO is also reported. In addition, a considerable amount of multiphase inclusions (complex), such as Al_2O_3-MnS, AlN-MnS, AlON, and AlON-MnS, has been observed.

During cooling of liquid steel, MnS precipitates on the existing inclusions resulting in the formation of complex MnS inclusions. In AHSS, these complex inclusions include Al_2O_3-MnS, AlN-MnS, and AlON-MnS. Park et al. [9] reported that in Fe-10Mn-yAl (y = 1, 3, and 6) steels ~20% to 40% of the total inclusions were complex MnS. In the work of Gigacher et al. [15] ~42% of the inclusions observed in TWIP steel with 25% Mn were duplex inclusions containing MnS. Alba et al. [12] studied the characteristics of inclusions in Fe-xMn-3Al-3Si (x = 2, 5 and 20) steels and found that the fraction of complex MnS inclusions increased from ~10% to over 70% with an increase in Mn content. The characteristics of complex MnS inclusions are related to the potency of different inclusion to serve as a nucleation site for MnS. In previous work, the authors [16] reported that the order of effectiveness of inclusions for the precipitation of MnS in AHSS is AlN > AlON > Al_2O_3.

The current work investigates the influence of Al and N contents of steel on the characteristics of complex MnS inclusions. Moreover, the effect of the cooling rate of steel samples is considered. For this purpose, Al content is varied from 0.5% to 6% (0.5, 1, 3, and 6) in Fe-5Mn-3Si-Al alloy, and samples from Fe-5Mn-3Si-3Al alloy containing different levels of N (<10 ppm to 54 ppm) are analyzed. Moreover, air cooled and furnace cooled samples obtained from these alloys are investigated to study the effect of cooling rate.

2. Materials and Methods

The experimental steels were produced in a vertical resistance tube furnace. The steels contain 0.5%, 1%, 3%, or 6% Al, 5% Mn, 3% Si, and 0.1% C. They are labeled based on their Mn, Al, and Si contents, i.e., 50.53, 513, 533, and 563. The reagents were melted in an alumina crucible at 1873 K under Ar atmosphere (5N purity). The Ar gas was passed through Ti turnings at 973 K to reduce oxygen from it. The molten steel was homogenized for 30 minutes, and then the system was evacuated and backfilled with Ar. Several quartz tube samples (Dia. = 5 mm, Length ≈ 8 mm) were taken at different holding times and were air cooled (20–30 K/sec [17]). The remaining steel material (bulk steel) was cooled along with the furnace at a rate of 10 °C/min (0.167 K/sec). The remaining bulk steel had a diameter of 58 mm, and its height was 30 mm. In another experiment, N_2 gas was introduced into a 533 steel. In this experiment (533N-P), the furnace chamber was evacuated at 1873 K, and then it was backfilled by purging a mixture of Ar and N_2 gas (1:1). The mixing ratio was changed to Ar:N_2 = 1:2 after 180 min of purging. Quartz tube samples were collected before and after purging the mixture of Ar and N_2 gas.

Induction coupled plasma optical emission spectrometry (ICP-OES) was used to analyze the chemical composition of steel samples. The oxygen-nitrogen and carbon-sulfur contents of samples were measured by LECO O/N (ON736, LECO Co. St. Joseph, MI, USA) and LECO C/S (CS744, LECO Co. St. Joseph, MI, USA) analyzer, respectively. Both air cooled quartz tube samples and furnace cooled bulk steel samples were analyzed for inclusions by using Jeol 6610 (Jeol Co. Akishima, Tokyo, Japan) scanning electron microscope (SEM) equipped with the ASPEX inclusion analysis system. The inclusions having a maximum diameter (D_{max}) > 2 μm were considered for analysis. A detailed description of experimental materials and procedure is presented elsewhere [18].

3. Results

An insignificant difference was observed in the chemical composition of all the samples taken during an experiment except 533N-P. A variation in the N content was observed in the samples of 533N-P due to the purging of N_2 gas. The average composition of the air cooled samples obtained during an experiment is given in Table 1. For the case of 533N-P, three samples were selected to represent different N contents, which are low N, medium N, and high N. The low N, medium N, and high N samples were obtained before introducing N_2 gas to the steel, 45 min, and 270 min after purging N_2 gas to the steel, respectively. It can be seen in Table 1 that the N content of 50.53, 513, 533, and 563 steel samples fall in the low N category (<10 ppm). The detected values for total O content were scattered and less than 10 ppm, which is close to the detection threshold. Further, it is expected to have ±2 ppm in the calibration of N and O analyses. Therefore, <10 ppm is used for representation. The composition of furnace cooled steel was similar to that of air cooled samples. In the case of 533N-P, the furnace cooled steel, and air cooled samples containing high N had a similar composition.

Table 1. The composition of experimental steels (wt %).

Steel		Mn	Al	Si	C	S (ppm)	N (ppm)	O (ppm)
50.53		4.8	0.4	3.2	0.1	21.6	<10	<10
513		4.8	0.9	3.2	0.1	26.0	<10	<10
533		4.9	2.8	3.2	0.1	23.4	<10	<10
563		5.2	5.7	3.2	0.1	29.5	<10	<10
533N-P	Low N	5.0	2.6	3.8	0.1	28	<10	<10
	Medium N						33	<10
	High N						54	<10

3.1. Characteristics of Complex MnS Inclusions

The inclusions are classified into four major classes, i.e., Al_2O_3, AlN, MnS, and Other. The Al_2O_3 inclusions are further classified into two subclasses, $Al_2O_{3(pure)}$ and Al_2O_3-MnS. The AlN class consists of four subclasses, i.e., $AlN_{(pure)}$, AlN-MnS, AlON-MnS, and AlON. The 'Other' class contains complex oxide inclusions, which do not fall in the aforementioned classes. The details of the classification rules of inclusion were explained elsewhere [18].

SEM images, along with elemental mappings, of typical complex MnS inclusions are shown in Figure 1. As can be seen in Figure 1a, Al and O are present in the core, while Mn and S are distributed along the periphery in the Al_2O_3-MnS inclusion. In the case of AlN-MnS inclusion (Figure 1b), MnS is located at the top of the AlN particle. Whereas a small portion of MnS is located between Al_2O_3 and AlN phases in AlON-MnS inclusions (Figure 1c).
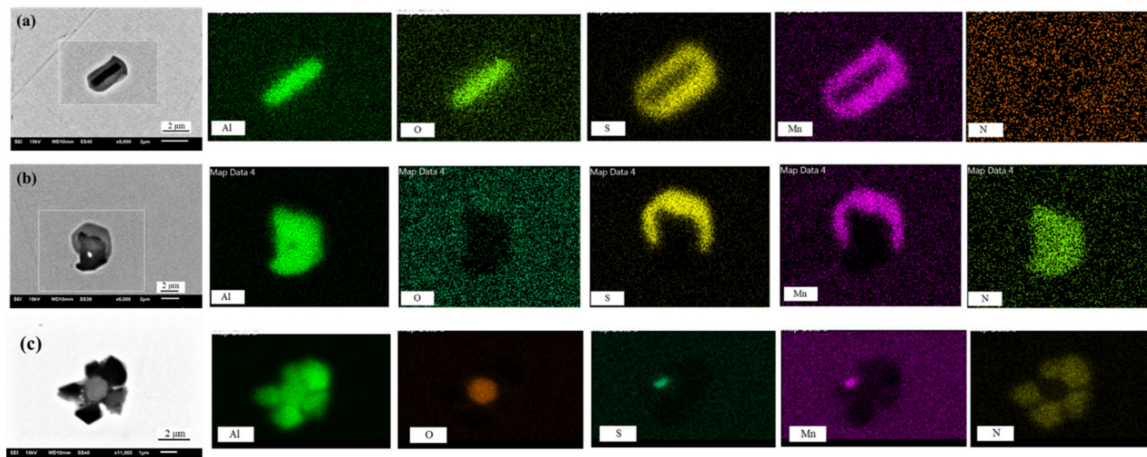
Figure 1. Typical examples of complex MnS inclusions, (**a**) Al2O3-MnS, (**b**) AlN-MnS, and (**c**) AlON-MnS.

Detailed inclusion analyses of the current experiments are presented and discussed elsewhere [19,20]. Figure 2 presents the number per unit area (N_A) of complex MnS inclusions observed in the air cooled samples of all experimental steels. As can be seen in Figure 2a, 50.53 steel contained ~2 mm^{-2} of complex MnS inclusions. Which slightly increased to ~2.7 mm^{-2} in 513 steel and then substantially increased to ~10 mm^{-2} in 533 steel. This value decreased to ~8 mm^{-2} with a further increase in Al content (563 steel). Figure 2b clearly indicates that an increase in the N content of steel resulted in a decrease in the amount of complex MnS inclusions from ~3.5 mm^{-2} to less than 1 mm^{-2}.
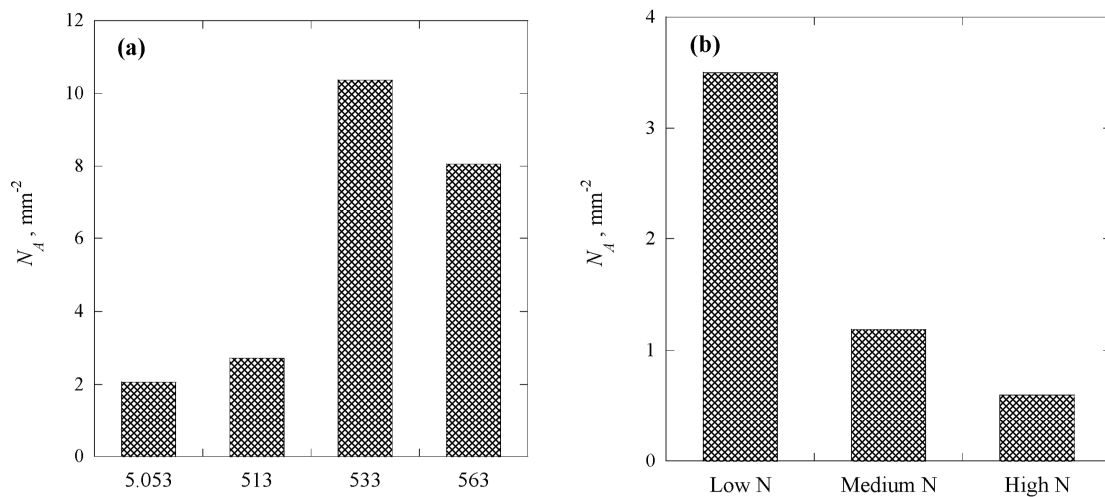
Figure 2. The number of complex MnS inclusions in air cooled samples (**a**) for varied Al content and (**b**) for varied N content of experimental steels.

The N_A of complex MnS inclusions observed in the furnace cooled samples from all experiments is shown in Figure 3. It can be seen that all steels contained almost a similar amount of complex MnS inclusions (between 8 and 10 mm^{-2}) despite the difference in Al and N content of steel samples. However, 513 and 533 steel samples have a relatively higher amount of complex MnS inclusions compared to those observed in other steels.
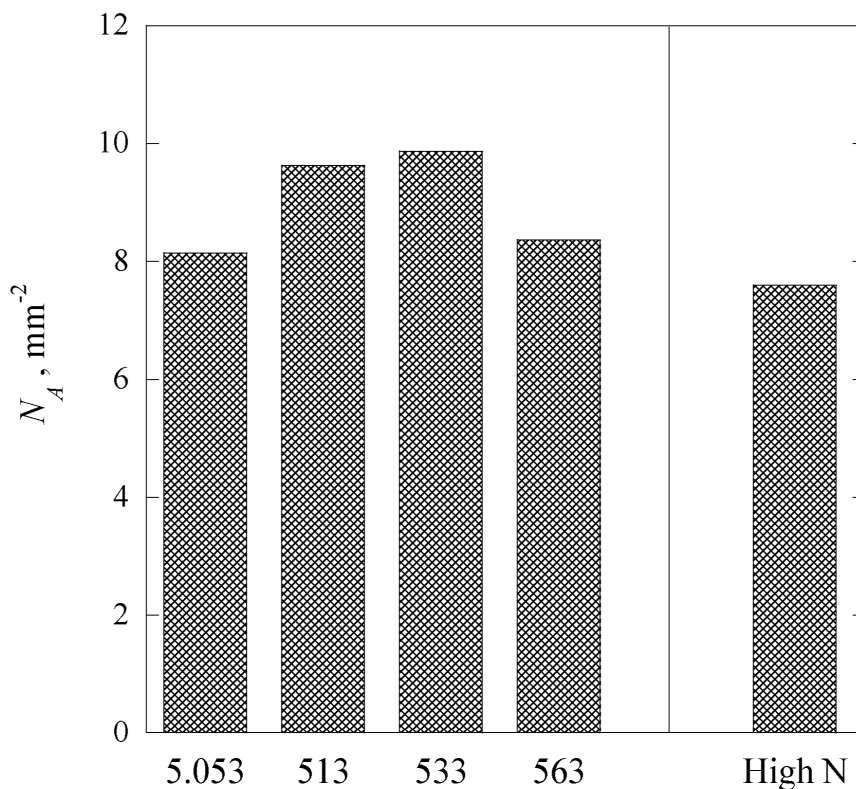
Figure 3. The number of complex MnS inclusions in furnace cooled samples of experimental steels.

Figure 4 depicts the distribution of complex MnS inclusions among different classes of inclusions observed in air cooled samples. As seen in Figure 4a, the fraction of MnS associated with Al$_2$O$_3$ (as in Al$_2$O$_3$-MnS) is highest in 50.53 steel, i.e., ~45%. An increase in Al content decreases the fraction of Al$_2$O$_3$-MnS. The 563 steel contains only ~8% of Al$_2$O$_3$-MnS inclusions. Around 52% of complex MnS

inclusions in 50.53 steel consist of AlN-MnS. This value increases to ~54% and ~68% as Al content increases to 1 and 3%, respectively. The fraction of AlON-MnS is lowest for 50.53 steel and is highest for 563 steel (31%), whereas that for 513 and 533 steels is 11% and 16%, respectively. In 533N-P steel, all samples with different N levels contain between ~60% and ~80% of AlN-MnS, see Figure 4b. The fraction of Al_2O_3-MnS and AlON-MnS varies from ~12% to ~22% without any clear trend. It can be inferred from Figure 4a that the contribution of Al_2O_3-MnS in complex MnS inclusions decreases with increasing Al content of steel, whereas that of AlN-MnS and AlON-MnS increases. However, it is debatable due to a low N_A value of complex MnS inclusions in 50.53 and 513 steels. Figure 4b suggests that the composition of complex MnS is independent of the N content of the steel. Again it should be noted that the N_A value of complex MnS inclusions in samples from 533N-P steel is small to confirm such a suggestion. Moreover, both Figure 4a,b indicate that in the air cooled samples, AlN-MnS inclusions make a higher portion of complex MnS inclusions as compared to that of Al_2O_3-MnS.
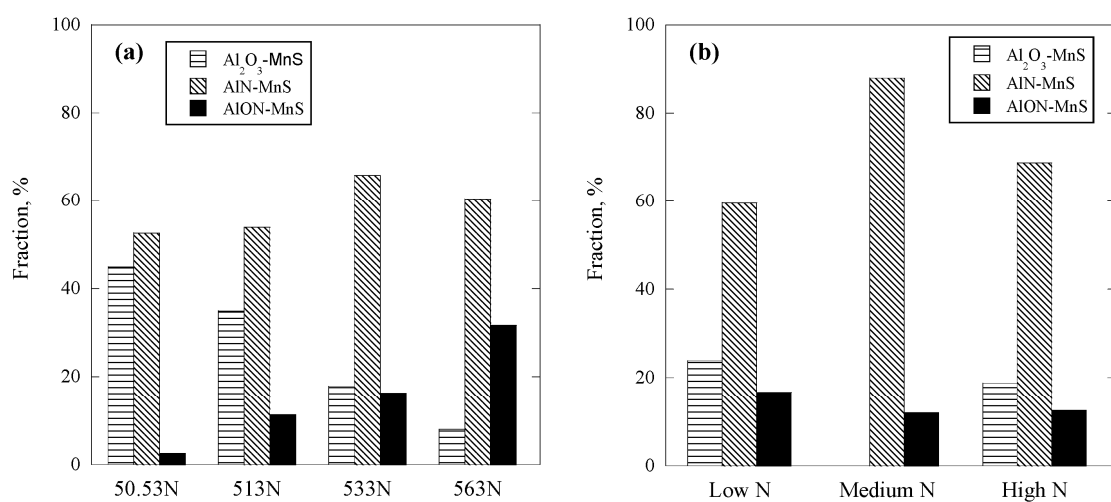
Figure 4. The composition of complex MnS inclusions observed in air cooled samples (**a**) varied Al content and (**b**) varied N content of experimental steels.

The composition of complex MnS inclusions observed in furnace cooled samples is presented in Figure 5. The results show that an increase in the Al content of steel leads to a decrease and an increase in the fraction of AlN-MnS and Al_2O_3-MnS inclusions, respectively. This tendency is opposite to that observed in the air cooled samples. The fraction of AlN-MnS inclusions decreases from ~50% to 22%, while that of Al_2O_3-MnS inclusions increases from ~36% to over 60%. Moreover, Al_2O_3-MnS inclusions have a higher fraction in complex MnS as opposed to AlN-MnS in the air cooled samples. The fraction of AlON-MnS does not vary much with Al content; however, it was generally higher than that in air cooled samples. The complex MnS inclusions in furnace cooled sample from 533N-P have a similar composition as that of its air cooled samples.
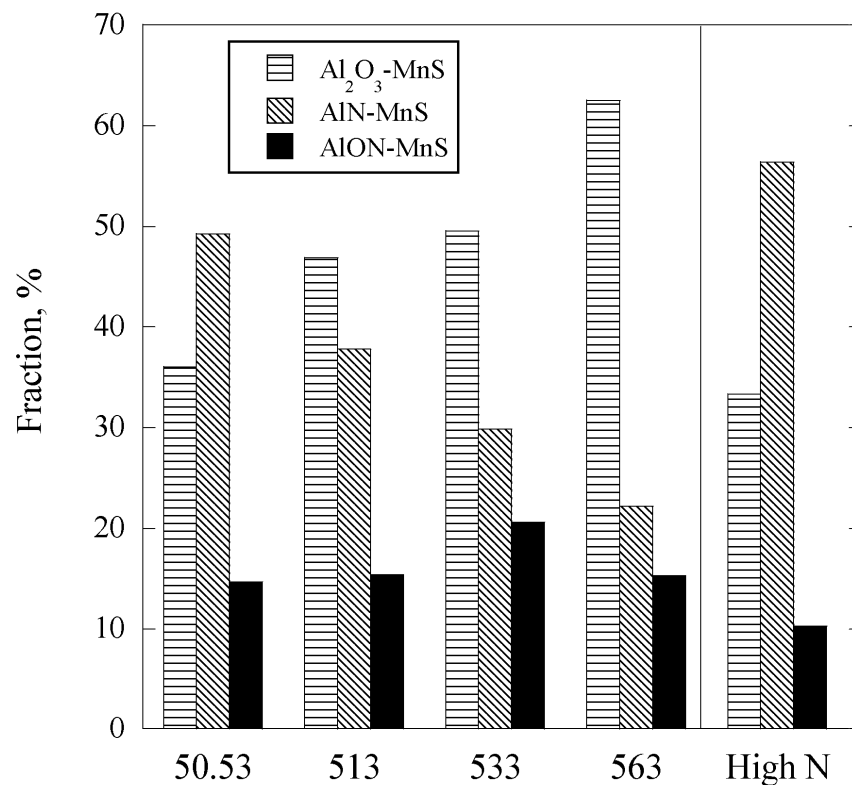
Figure 5. The composition of complex MnS inclusions observed in furnace cooled samples of experimental steels.

3.2. MnS Precipitation Ratio

The tendencies observed in Figures 3 and 4 are further quantified by determining the ratio of MnS precipitated on different types of inclusions. MnS precipitation ratio on a specific type of inclusion is defined as the ratio of the number of MnS containing particles to all of the particles in that type of inclusions. For example, the MnS precipitation ratio (PR_{MnS}) for AlN inclusions is calculated as follows:

$$PR_{MnS} = \frac{n_{AlN-MnS}}{n_{AlN-MnS} + n_{AlN_{(pure)}}} \times 100\% \tag{1}$$

where, $n_{AlN-MnS}$ and $n_{AlN_{(pure)}}$ represent the number of AlN-MnS inclusions and the number of $AlN_{(pure)}$ inclusions, respectively. Similar equations can be written for the MnS precipitation ratio for Al_2O_3 and AlON inclusions. The calculated PR_{MnS} for AlN, Al_2O_3, and AlON inclusions observed in air cooled samples is given in Figure 6. As demonstrated in Figure 6a, the PR_{MnS} for Al_2O_3 inclusions is the least (<20%), and that of AlON is between 30% and 40%. The PR_{MnS} for AlN inclusions is almost 100% for 50.53, 513, and 533 steels, and it is relatively less for 563 steel, i.e., ~63%. Figure 6b shows that the low N sample of 533N-P steel exhibits similar PR_{MnS} values as observed for 533 steel, which also has a low N content. The PR_{MnS} values for all three types of inclusions significantly decreased to less than 10%, with an increase in the N content of 533N-P steel samples. A high PR_{MnS} value for a particular type of inclusions means that a higher fraction of those inclusions coexists with MnS. For instance, almost all the AlN type inclusions in a low N sample of 533N-P steel are AlN-MnS. Whereas, the very low PR_{MnS} value for medium N and high N level samples indicates that almost all the AlN type inclusions in these samples are $AlN_{(pure)}$.
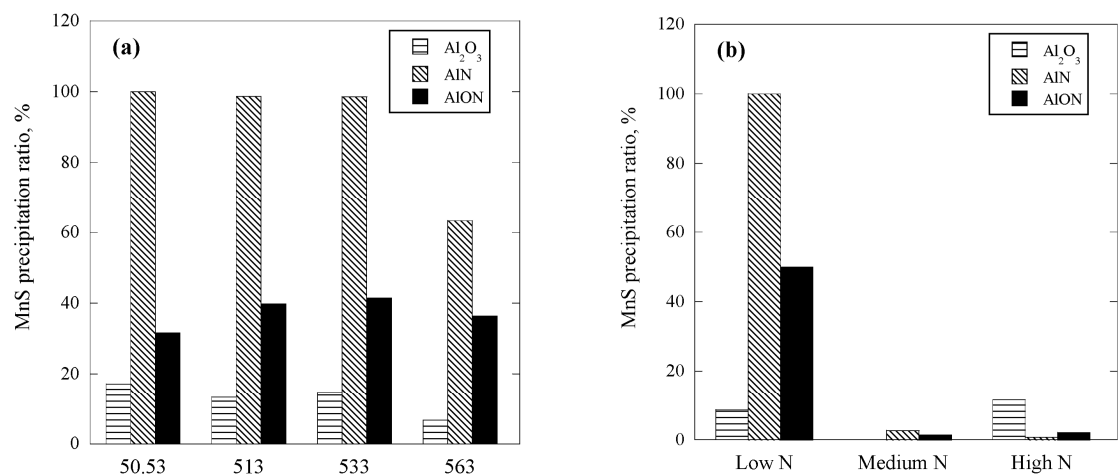
Figure 6. Comparison of MnS precipitation ratio of different types of inclusions in the air cooled samples (**a**) varied Al content and (**b**) varied N content of steel.

The calculated PR_{MnS} values of the furnace cooled samples are shown in Figure 7. It is notable that in the furnace cooled samples, the PR_{MnS} values for Al_2O_3 inclusions are around 80% for all the samples, which is significantly higher than that observed in air cooled samples. Moreover, those for AlON have increased more than two times. On the contrary, the PR_{MnS} values for AlN have decreased (except 533N-P) compared to those observed in Figure 6. For 50.53 and 513, the value dropped from ~100% to ~80%. A decrease of ~37% and ~25% is observed in the PR_{MnS} values of 533, and 563 steel as compared to their respective values in the air cooled samples. The furnace cooled sample of 533N-P is to be compared to its high N level air cooled sample because of their similar N content. The furnace cooled sample has a higher PR_{MnS} value for AlN as compared to that in air cooled one (compare Figures 6b and 7).
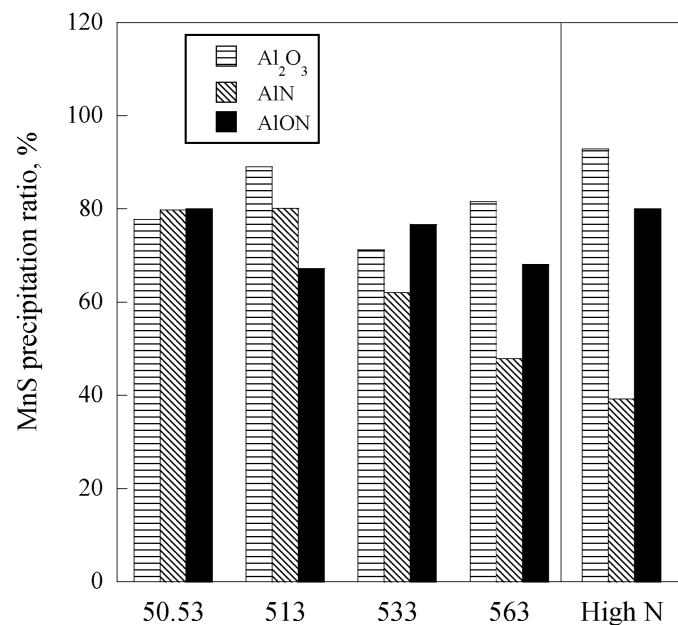
Figure 7. Comparison of MnS precipitation ratio of different types of inclusions in the furnace cooled samples of experimental steels.

The higher PR_{MnS} values for AlN in the air cooled samples and for Al_2O_3 in the furnace cooled samples support the inference deduced from Figures 4 and 5 i.e., complex MnS inclusions in the air

cooled samples contain a higher fraction of AlN-MnS, and Al_2O_3-MnS make a significant fraction of those in furnace cooled samples. However, the influence of Al content seen in Figure 4 is not reflected in Figure 6.

4. Discussion

The following three factors are to be considered for understanding the tendencies observed in Figure 4 through Figure 7.

4.1. Thermodynamics of Inclusions Formation

Thermodynamic calculations were carried out by using Factsage 7.3 (CRCT, Montreal, QC, Canada and GTT-Technologies, Aachen, Germany) to determine the stable phases in the current steel compositions for a temperature range between 1473 K and 1873 K. It was found that at 1873 K Al_2O_3 is the only stable phase for all steel compositions except for a high N sample of 533N-P steel. For a high N sample, both Al_2O_3 and AlN are stable at working temperature. In addition to phase stability, the liquidus temperature (T_{liq}), solidus temperature (T_{sol}), AlN formation temperature (T_{AlN}), and MnS formation temperature (T_{MnS}) were also determined. The obtained data is presented in Table 2. The T_{AlN} values for 563 and medium N sample of 533N-P are higher than their respective T_{liq} values, indicating that for these two compositions, AlN starts to form before the solidification begins during cooling. Whereas, the T_{AlN} values for the remaining four compositions suggest that AlN forms during the solidification of steel. This is because the driving force of AlN formation increases during solidification due to the enrichment of Al and N at the solidification front. The Scheil equation [11,13,21] was used to calculate the concentration of [%Al] and [%N] in the liquid phase at the solidifying front. The equations for [%Al] and [%N] are given below.

$$[\%Al] = [\%Al]_0 (1 - g_s)^{(k_{Al} - 1)} \tag{2}$$

$$[\%N] = \frac{[\%N]_0}{k_N + (1 - k_N)(1 - g_s)} \tag{3}$$

where g_s is the solid fraction, and $[\%Al]_0$ and $[\%N]_0$ are the initial weight percentages of solute Al and N in liquid steel, respectively. k_{Al} (= 0.6) and k_N (= 0.27) are the equilibrium partition ratios of solute Al and N, respectively [21,22]. The equilibrium constant for formation of AlN ($K_{AlN} = [\%Al] \times [\%N]$) can be calculated according to Equation (4) [23].

$$K_{AlN} = 10^{-\frac{15850.93}{T} + 7.0297} \tag{4}$$

Table 2. Thermodynamic data for all the experimental steels.

	Steel	T_{sol} (K)	T_{liq} (K)	T_{AlN} (K)	T_{MnS} (K)
	50.53	1647.3	1739.5	1585.6	1528.9
	513	1629	1739.5	1643.3	1499.6
	533	1619.4	1735.5	1696.7	1464.5
	563	1605.9	1722.1	1723.6	1466.7
	Low N	1611	1726.3	1679.1	1472.8
533N-P	Medium N	1611	1726.3	1865.4	1473.9
	High N	1611	1726.3	1879.5	1473.9

The relationship between the temperature at the solidifying front (T') and the solid fraction (g_s) is shown in Equation (5) [11].

$$T' = T_m - \frac{T_m - T_{liq}}{1 - g_s \frac{T_{liq} - T_{sol}}{T_m - T_{sol}}} \tag{5}$$

where T_m, T_{sol}, and T_{liq} are the melting temperature of pure Fe (1811 K, 1538 °C), the solidus temperature of steel, and the liquidus temperature of steel, respectively.

Using Equations (2)–(5), a relationship between [%Al] × [%N] at solidification front and g_s, and equilibrium value for AlN formation (K_{AlN}) and g_s can be obtained. An intersection of both functions gives the g_s value at which AlN formation starts. The obtained results for the current experimental steels are given in Table 3. For calculation of g_s values, N content is assumed to be 10 ppm. The results indicate the AlN starts to form at a g_s of 0.85 for 50.053 steel. Moreover, AlN formation takes place at an early stage of solidification, i.e., at lower g_s values in 513 and 533.

Table 3. The calculated solid fraction values for the formation of AlN.

| 50.53 | 513 | 533 | 563 | 533N-P | | |
				Low N	Medium N	High N
0.85	0.69	0.22	-	0.11	-	-

4.2. Heterogeneous Nucleation of Inclusions

Inclusions in steel can homogeneously nucleate in the melt or heterogeneously on the existing solid particles or matrix. Heterogeneous nucleation is more likely to take place as it requires a less nucleation energy. The morphology of complex MnS inclusions (Figure 1) observed in the current study suggests they are formed due to heterogeneous nucleation of MnS on other inclusions. The heterogeneous nucleation is influenced by several factors, among them, the lattice misfit or disregistry between the substrate and nucleated phase has a significant contribution [24,25]. The lattice misfit or disregistry determines the effectiveness of an inclusion to act as a nucleus for another. It is suggested that an inclusion can act as an effective nucleation site for a solid phase when the lattice misfit between the substrate inclusion and nucleated solid is less than 12% [24]. A higher value means less effectiveness as nucleant.

The lattice misfit can be calculated as follows [26]:

$$Misfit = \frac{|a_n - a_s|}{a_s} \times 100\% \tag{6}$$

where a_n and a_s are the lattice parameters of nucleated solid and substrate, respectively.

Table 4 presents the lattice parameters used for misfit calculations. The calculated misfit between MnS and Al_2O_3 (substrate) is ~10% along *a* axis. Whereas, MnS nucleation on the *c* axis of AlN gives a misfit of ~5%. These values are in agreement with those reported by Ohta and Suito [27]. A lower mismatch value for AlN means that less interfacial energy is required for nucleation of MnS on AlN compared to that on Al_2O_3; hence, MnS would preferentially nucleate on AlN. This explains a significantly higher MnS precipitation ratio for AlN inclusions in the experimental steels.

Table 4. The lattice parameters used for misfit calculations [28,29].

| Inclusion | Lattice Parameters (Å) | | |
	a	*b*	*c*
Al_2O_3	4.75	4.75	12.99
AlN	3.11	3.11	4.99
MnS	5.24	5.24	5.24

Similar to Al_2O_3-MnS and AlN-MnS inclusions, AlON-MnS complex inclusions are formed by heterogeneous nucleation of MnS on AlON inclusions. Here it is important to mention that the AlON inclusions observed in the current study are not single AlON phase inclusions rather they consist of distinct Al_2O_3 and AlN phases (see Figure 1c). Moreover, it is reported that the AlON phase is stable only above 1923 K (1650 °C), and below this temperature, it dissociates into AlN+Al_2O_3 [30]. Based on the thermodynamic stability of AlON (single phase), Al_2O_3, and AlN phases, it can be implied that the observed AlON inclusions are a result of AlN nucleation on existing Al_2O_3 inclusions. The calculated lattice misfit between (*a* axis of) AlN and Al_2O_3 is about 35%. However, a 30° in-plane rotation of AlN with respect to Al_2O_3 reduces this misfit to ~12% [31,32]. A 12% misfit means that Al_2O_3 is not a very effective substrate for nucleation of AlN, but it can still occur particularly in the presence of high Al content of the steel. The effect of Al content on the formation of AlON is reflected in Figure 4b, which shows that the fraction of AlON-MnS in complex MnS inclusions increases with Al content of the steel. Hence, the formation of AlON-MnS inclusions takes place by duplex heterogeneous nucleation. First, AlN nucleates on Al_2O_3, then MnS heterogeneously nucleates on AlN (or Al_2O_3 but preferentially on AlN).

4.3. Inclusion Behavior at Solid/Liquid Interface

It is established in the preceding sections that for most of the investigated steel compositions, complex MnS inclusions are formed during the solidification of steel and by heterogeneous nucleation of MnS on already existing inclusions. Therefore, the behavior of nucleant inclusions at the solidification front is considered. During the solidification of liquid steel, inclusions are either engulfed or pushed by the solid/liquid interface. There are several factors that determine the inclusion behavior at solid/liquid interface, such as solidification velocity, interfacial energy between inclusion and liquid steel, the viscosity of steel, size of the particle, and thermal conductivity of inclusion and steel. Stefanescu et al. [33] derived a relationship describing the critical velocity, V_{CR}, of solid/liquid interface to determine engulfment/pushing transition. A solidification velocity higher than V_{CR} would result in the engulfment of inclusions of a specific size. The relationship is expressed as follows:

$$V_{CR} = \left(\frac{\Delta\gamma_o \,.a_o^2}{3.\eta.k^*.R} \right)^{\frac{1}{2}} \tag{7}$$

where a_o is the atomic distance (m), η is the viscosity of liquid steel (kg/ms), and R is the radius of particle (m). k^* is the ratio of the thermal conductivities of the particle (k_P) and liquid steel (k_L), i.e., $k^* = \frac{k_P}{k_L}$. $\Delta\gamma_o$ is given as follows:

$$\Delta\gamma_o = \gamma_{PS} - (\gamma_P - \gamma_L.cos\,°\theta_{PL}) \tag{8}$$

$$\gamma_{PS} = \gamma_P + \gamma_S - W_{AD} \tag{9}$$

where γ_{PS} is the interfacial energy between particle and liquid steel (J/m^2). γ_P, γ_L, and γ_S are the surface energies of the particle, liquid steel, and solid steel, respectively (J/m^2). θ_{PL} is the contact angle and W_{AD} is the work of adhesion.

In the current study, Equation (7) is adopted to determine the relationship between V_{CR} and the size of inclusion for Al_2O_3 and AlN. The parameters used to determine the relationship are given in Table 5. The data used for calculating $\Delta\gamma_o$ of AlN comes from the work of Y. Luo [34], where the AlN substrate was produced using Y_2O_3 as a binder. The a_o value for both Al_2O_3 and AlN is taken as the atomic diameter of aluminum [33]. The obtained results are plotted in Figure 8. It is evident from the figure that there exists a difference in the behavior of Al_2O_3 and AlN inclusions at the solid/liquid interface. Figure 8 suggests that AlN inclusions are more likely to be engulfment by the solidification front as compared to Al_2O_3 inclusions at a certain solidification velocity. For instance, AlN inclusions with diameter > ~1 μm would be engulfed at a solidification velocity of 4×10^{-6} m/s, and only

inclusions with diameter < 1 μm would be pushed. Whereas, Al_2O_3 inclusions with diameter up to ~3.5 μm can be pushed by the solidification front for the same solidification velocity.

Table 5. Parameters used for the calculation of critical velocity.

	Al_2O_3	Reference	AlN	Reference
η (kg/ms)	4×10^{-6}	[35]	4×10^{-6}	[35]
γ_P (J/m^2)	0.75	[36]	1.53	-
γ_L (J/m^2)	1.6	[37]	1.6	[37]
γ_S (J/m^2)	2.206	[33]	2.206	[33]
γ_{PS} (J/m^2)	2.56	-	3.49	-
γ_{PL} (J/m^2)	1.88	-	2.54	[34]
θ_{PL}	135	[33]	129	[34]
W_{AD} (J/m^2)	0.39	[38]	0.24	[34]
$\Delta\gamma_o$	0.68	-	0.953	-
k_P (W/mK)	5.5	[33,36]	24	[39]
k_L (W/mK)	45	[33,35]	45	[33,35]
a_o (m)	2.5×10^{-10}	[33]	2.5×10^{-10}	[33]

The values without references are calculated using other data given in Table 5.
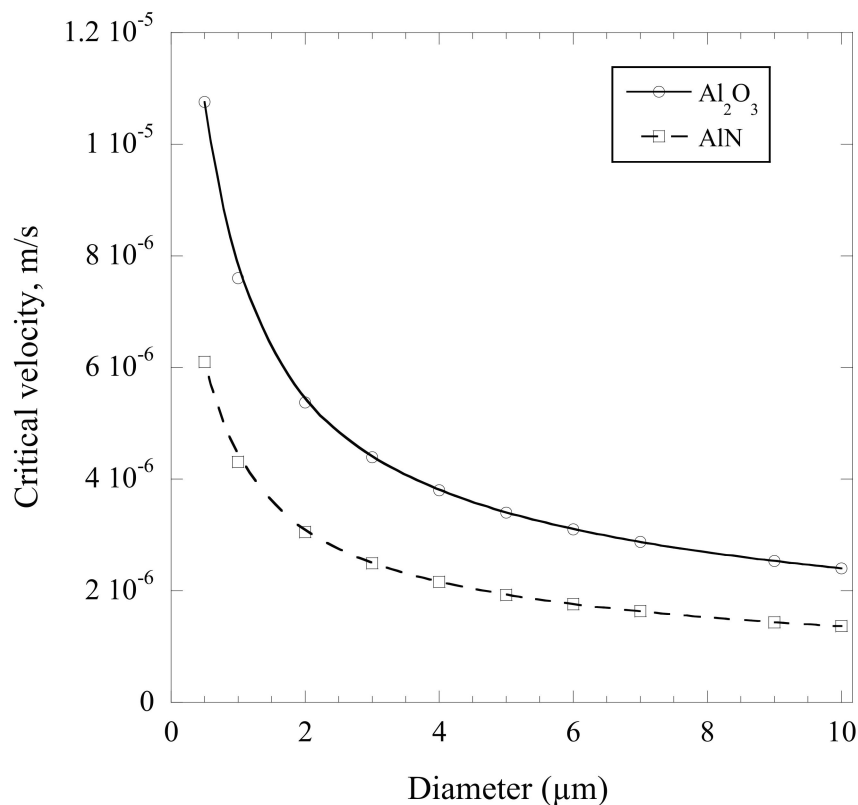
Figure 8. The calculated correlation between critical velocity and size of inclusions for pushing/engulfment transition of Al_2O_3 and AlN inclusions.

The difference in the PR_{MnS} values of different types of inclusions observed in the air cooled samples (Figure 6) is related to lattice misfit. The low effectiveness (high misfit) of Al_2O_3 for the nucleation site of MnS is the reason for the low PR_{MnS} values for Al_2O_3, Figure 6. AlN inclusions

have higher PR_{MnS} values due to a low lattice misfit between AlN and MnS. Considering this and the stability of AlN in the medium N and high N containing samples of 533N-P, it can be argued that these samples should also have high PR_{MnS} values for AlN. However, AlN inclusions have very low PR_{MnS} values (<5%) in these samples (Figure 6b). This phenomenon suggests that only the AlN inclusions which are formed at the solidification front, or closer to the formation of MnS, participate in heterogeneous nucleation of MnS. This behavior is also reflected in the air cooled sample of 563 steel (Figure 6a), where the PR_{MnS} value for AlN is relatively lower because the formation of AlN starts above T_{liq} (Table 2).

In all the furnace cooled samples (except for 533N-P), the PR_{MnS} values for AlN decrease in comparison to those of air cooled samples. This can also be explained by considering the formation of AlN-MnS inclusions at the solidification front. However, due to the slow cooling rate, the AlN inclusions which form at the early stage of solidification are engulfed by the solidification front as $AlN_{(pure)}$ inclusions. Hence, lower PR_{MnS} values for AlN are observed in furnace cooled samples. This reasoning also explains relatively lower PR_{MnS} values for AlN in 533 (~60%) and 563(~40%) furnace cooled samples as compared to those of 50.53 and 533 (~80%), see Figure 7. A higher number of $AlN_{(pure)}$ inclusions would form in 533 and 563 due to their low g_s values for AlN formation; hence, low PR_{MnS} values for AlN in these steels. An even lower PR_{MnS} value for furnace cooled sample 533N-P affirms this logic, as $AlN_{(pure)}$ inclusions start to form in liquid steel for this sample.

Moreover, Al_2O_3 inclusions have significantly higher (~80%) PR_{MnS} values in furnace cooled samples as compared to less than 10%, as observed in air cooled samples. As shown in Figure 8, Al_2O_3 inclusions can be easily pushed (compared to AlN) to the liquid ahead of the solidification front, especially at low solidification velocities. Moreover, Al_2O_3 inclusions can also form during solidification. Therefore, a higher quantity of Al_2O_3 inclusions are present in solute enriched liquid; thereby, higher PR_{MnS} values for Al_2O_3 inclusions. The end of solidification liquid enriched in Al_2O_3 and solute elements also means an increase in the formation of AlON inclusions and their increased PR_{MnS} values (compare Figures 6 and 7 for AlON).

The differences in the composition of complex MnS inclusions of air cooled and furnace cooled samples, as shown in Figures 4 and 5, are also attributed to the lattice misfit of inclusions with MnS and their behavior at the solid/liquid interface.

5. Conclusions

In the present study, laboratory experiments were carried out to investigate the characteristics of complex MnS inclusions in AHSS and their formation behavior. The following observations were made.

The number of complex MnS inclusions increases with an increase in Al content of steel, and it decreases with an increase in N content.

Under air cooling condition, an increase in the Al content of steel results in an increase and a decrease in Al_2O_3-MnS and AlN-MnS inclusions, respectively. Whereas, N content does not have any specific relation to the composition of complex MnS inclusions.

Under furnace cooled conditions, the complex MnS inclusions become rich in Al_2O_3-MnS as Al content of steel increases; meanwhile, the portion of AlN-MnS decreases.

The effectiveness of inclusions for the precipitation of MnS is related to their lattice misfit with MnS, and its order is AlN > AlON > Al_2O_3.

The precipitation ratio of MnS for AlN is influenced by the stability of AlN in liquid steel, i.e., it decreases when AlN can form in liquid steel before solidification starts.

Slow cooling significantly increases the MnS precipitation for Al_2O_3 and AlON, and slightly decreases that for AlN. It is attributed to the difference in the pushing and engulfment behavior of Al_2O_3 and AlN.

References

1. Penna, R.V.; Bartlett, L.N.; Constance, T. Understanding the Role of Inclusions on the Dynamic Fracture Toughness of High Strength Lightweight FeMnAl Steels. *Int. J. Met.* **2018**, *13*, 286–299. [CrossRef]
2. Li, D.Z.; Wei, Y.H.; Xu, B.S.; Hou, L.F.; Han, P.D. Development in fundamental research on TWIP steel used in automobile industry. *Ironmak. Steelmak.* **2011**, *38*, 540–545. [CrossRef]
3. Aydin, H.; Essadiqi, E.; Jung, I.-H.; Yue, S. Development of 3rd generation AHSS with medium Mn content alloying compositions. *Mater. Sci. Eng. A* **2013**, *564*, 501–508. [CrossRef]
4. Steenken, B.; Rezende, J.L.L.; Senk, D. Hot ductility behaviour of high manganese steels with varying aluminium contents. *Mater. Sci. Technol.* **2016**, *33*, 567–573. [CrossRef]
5. Yang, J.; Wang, Y.N.; Ruan, X.M.; Wang, R.Z.; Zhu, K.; Fan, Z.J.; Wang, Y.C.; Li, C.B.; Jiang, X.F. Effects of Manganese Content on Solidification Structures, Thermal Properties, and Phase Transformation Characteristics in Fe-Mn-Al-C SteelsMetall. *Mater. Trans. B Process Metall. Mater. Process. Sci.* **2015**, *46*, 1365–1375. [CrossRef]
6. Liu, H.; Liu, J.; Wu, B.; Shen, Y.; He, Y.; Ding, H.; Su, X. Effect of Mn and Al contents on hot ductility of high alloy Fe-xMn-C-yAl austenite TWIP steels. *Mater. Sci. Eng. A* **2017**, *708*, 360–374. [CrossRef]
7. Lucaci, M.; Lungu, M.; Vasile, E.; Marinescu, V.; Talpeanu, D.; Sbarcea, G.; Stancu, N.; Ivan, I.; Alexandru, I.; National Institute for Research and Development in Electrical Engineering ICPE-CA (INCDIE ICPE-CA); et al. Advanced High Strength Steel (AHSS) Alloys. *J. Am. Romanian Acad. Arts Sci.* **2017**, *1*, 46–50. [CrossRef]
8. Hu, B.; Luo, H.; Yang, F.; Dong, H. Recent progress in medium-Mn steels made with new designing strategies, a review. *J. Mater. Sci. Technol.* **2017**, *33*, 1457–1464. [CrossRef]
9. Park, J.H.; Kim, D.-J.; Min, D.J. Characterization of Nonmetallic Inclusions in High-Manganese and Aluminum-Alloyed Austenitic Steels. *Met. Mater. Trans. A* **2012**, *43*, 2316–2324. [CrossRef]
10. Zhuang, C.; Liu, J.; Mi, Z.; Jiang, H.-T.; Tang, D.; Wang, G. Non-Metallic Inclusions in TWIP Steel. *Steel Res. Int.* **2014**, *85*, 1432–1439. [CrossRef]
11. Liu, H.; Liu, J.; Michelic, S.; Wei, F.; Zhuang, C.; Han, Z.; Li, S. Characteristics of AlN inclusions in low carbon Fe–Mn–Si–Al TWIP steel produced by AOD-ESR method. *Ironmak. Steelmak.* **2016**, *43*, 171–179. [CrossRef]
12. Alba, M.; Nabeel, M.; Dogan, N. Investigation of Inclusion Formation in Light-Weight Fe–Mn–Al Steels using Automated Scanning Electron Microscope Equipped with Energy-Dispersive X-Ray Spectroscopy. *Steel Res. Int.* **2019**, *91*. [CrossRef]
13. Nabeel, M.; Alba, M.; Karasev, A.; Jönsson, P.G.; Dogan, N. Characterization of Inclusions in 3rd Generation Advanced High-Strength Steels. *Met. Mater. Trans. A* **2019**, *50*, 1674–1685. [CrossRef]
14. Kong, L.; Deng, Z.; Zhu, M. Formation and Evolution of Non-metallic Inclusions in Medium Mn Steel during Secondary Refining Process. *ISIJ Int.* **2017**, *57*, 1537–1545. [CrossRef]
15. Gigacher, G.; Krieger, W.; Scheller, P.R.; Thomser, C. Non-Metallic Inclusions in High-Manganese-Alloy Steels. *Steel Res. Int.* **2005**, *76*, 644–649. [CrossRef]
16. Nabeel, M.; Alba, M.; Dogan, N. Formation behavior of complex MnS inclusions in AHSS. unpublished, manuscript in preparation.
17. Ericsson, O.T.; Lionet, M.; Karasev, A.V.; Inoue, R.; Jönsson, P.G. Changes in inclusion characteristics during sampling of liquid steel. *Ironmak. Steelmak.* **2012**, *39*, 67–75. [CrossRef]

18. Nabeel, M.; Alba, M.; Sun, S.; Karasev, A.; Jonsson, P. Characterization of Inclusions in High Mn Steel using Two-Dimensional and Three-Dimensional Methods. In Proceedings of the AISTech 2018, Philadelphia, PA, USA, 7–10 May 2018; pp. 1483–1491.

19. Alba, M.; Nabeel, M.; Dogan, N. Effect of aluminium content on the formation of inclusions in Fe–5Mn–xAl steels. *Ironmak. Steelmak.* **2020**, 1–8. [CrossRef]

20. Alba, M.; Nabeel, M.; Dogan, N. Effect of Nitrogen Content on the Formation of Inclusions in Fe-5Mn-3Al Steels. *Crystals* **2020**, *10*, 836. [CrossRef]

21. Paek, M.-K.; Jang, J.-M.; Jiang, M.; Pak, J.-J. Thermodynamics of AlN Formation in High Manganese-Aluminum Alloyed Liquid Steels. *ISIJ Int.* **2013**, *53*, 973–978. [CrossRef]

22. Turkdogan, E.T. *Fundamentals of Steelmaking*; The Institute of Materials: London, UK, 1996.

23. Paek, M.-K.; Jang, J.-M.; Kang, H.-J.; Pak, J.-J. Reassessment of AlN(s)=Al+N Equilibration in Liquid Iron. *ISIJ Int.* **2013**, *53*, 535–537. [CrossRef]

24. Bramfitt, B.L. The effect of carbide and nitride additions on the heterogeneous nucleation behavior of liquid iron. *Met. Mater. Trans. A* **1970**, *1*, 1987–1995. [CrossRef]

25. Turnbull, D.; Vonnegut, B. Nucleation Catalysis. *Ind. Eng. Chem.* **1952**, *44*, 1292–1298. [CrossRef]

26. Wang, F.; Fan, Z. Characterization of AlN Inclusion Particles Formed in Commercial Purity Aluminum. *Met. Mater. Trans. A* **2019**, *50*, 2519–2526. [CrossRef]

27. Ohta, H.; Suito, H. Precipitation and Dispersion Control of MnS by Deoxidation Products of ZrO2, Al2O3, MgO and MnO–SiO2 Particles in Fe–10mass%Ni Alloy. *ISIJ Int.* **2006**, *46*, 480–489. [CrossRef]

28. Sun, G.; Tao, S. Duplex Heterogeneous Nucleation Behavior of Precipitates in C-Mn Steel Containing Sn. *Met. Mater. Trans. A* **2018**, *49*, 519–523. [CrossRef]

29. Tuling, A.; Mintz, B. Crystallographic and morphological aspects of AlN precipitation in high Al, TRIP steels. *Mater. Sci. Technol.* **2015**, *32*, 568–575. [CrossRef]

30. Willems, H.; Hendrix, M.; De With, G.; Metselaar, R. Thermodynamics of Alon II: Phase relations. *J. Eur. Ceram. Soc.* **1992**, *10*, 339–346. [CrossRef]

31. Dovidenko, K.; Oktyabrsky, S.; Narayan, J.; Razeghi, M. Aluminum nitride films on different orientations of sapphire and silicon. *J. Appl. Phys.* **1996**, *79*, 2439–2445. [CrossRef]

32. Sun, C.J.; Kung, P.; Saxler, A.; Ohsato, H.; Haritos, K.; Razeghi, M. A crystallographic model of (00·1) aluminum nitride epitaxial thin film growth on (00·1) sapphire substrate. *J. Appl. Phys.* **1994**, *75*, 3964–3967. [CrossRef]

33. Stefanescu, D.M.; Catalina, A.V. Calculation of the Critical Velocity for the Pushing/Engulfment Transition of Nonmetallic Inclusions in Steel. *ISIJ Int.* **1998**, *38*, 503–505. [CrossRef]

34. Luo, Y.; Li, M.; Scheller, P.R.; Sridhar, S.; Zhang, L. Interaction Between Liquid Steel and AlN Substrate Containing Al-Y-Oxides. *Met. Mater. Trans. A* **2019**, *50*, 2459–2470. [CrossRef]

35. Ohta, H.; Suito, H. Effect of Sulfur and Oxygen on Engulfment and Pushing of Deoxidation Particles of ZrO2 and Al2O3 during Solidification of Fe–10mass%Ni Alloy. *ISIJ Int.* **2006**, *46*, 472–479. [CrossRef]

36. Shibata, H.; Yin, H.; Yoshinaga, S.; Emi, T.; Suzuki, M. In-situ Observation of Engulfment and Pushing of Nonmetallic Inclusions in Steel Melt by Advancing Melt/Solid Interface. *ISIJ Int.* **1998**, *38*, 149–156. [CrossRef]

37. Mu, W.; Dogan, N.; Coley, K.S. Agglomeration of Non-metallic Inclusions at the Steel/Ar Interface: Model Application. *Met. Mater. Trans. A* **2017**, *48*, 2092–2103. [CrossRef]

38. Keene, B.J. *Slag Atlas*, 2nd ed.; Verein Deutscher Eisenhüttenleute, Ed.; Verlag Stahleisen GmbH: Düsseldorf, Germany, 1995; p. 526.

39. Slack, G.A.; Tanzilli, R.; Pohl, R.; Vandersande, J.W. The intrinsic thermal conductivity of AlN. *J. Phys. Chem. Solids* **1987**, *48*, 641–647. [CrossRef]